Journal of Materials Chemistry B

Accepted Manuscript

ROYAL SOCIETY OF CHEMISTRY

www.rsc.org/materialsB

Superparamagnetic iron-doped nanocrystalline apatite as delivery system for doxorubicin

Michele Iafisco[†]*, Christophe Drouet[‡]*, Alessio Adamiano[†], Patricia Pascaud[‡§], Monica Montesi[†], Silvia Panseri[†], Stephanie Sarda[‡] and Anna Tampieri[†]

[†]Institute of Science and Technology for Ceramics (ISTEC), National Research Council (CNR), Via Granarolo 64, 48018 Faenza, Italy

[‡]CIRIMAT Carnot Institute, University of Toulouse, UMR CNRS/INPT/UPS 5085, Ensiacet, 4 allée Emile Monso, 31030 Toulouse Cedex 4, France

[§]Present address: University of Limoges, CNRS, SPCTS UMR 7315, CEC, 12 Rue Atlantis, 87068 Limoges Cedex, France

Author for correspondence:

Dr. Michele Iafisco
Institute of Science and Technology for Ceramics (ISTEC) National Research Council (CNR),
Via Granarolo 64, 48018 Faenza (RA), Italy.
E-mail: michele.iafisco@istec.cnr.it
Tel: +39 0546699730

Dr. Christophe Drouet
CIRIMAT Carnot Institute, University of Toulouse, UMR CNRS/INPT/UPS 5085,
Ensiacet, 4 allée Emile Monso, 31030 Toulouse cedex 4, France
E-mail: christophe.drouet@ensiacet.fr
Tel: +33 0534323411

Abstract

The development of non-toxic and biodegradable magnetic nanoparticles (NPs) that can be easily functionalized with drug or biomolecules and employed, under magnetic fields, as targeted nano-carriers or as components of scaffolds with on-demand functionalities, is a big challenge in the biomaterials research. In the present work the feasibility of previously synthesized iron-doped superparamagnetic apatite (FeHA) NPs to bind, and then to release under an applied low-frequency pulsed electromagnetic field (PEMF), the anticancer drug doxorubicin (DOX) was investigated. The behavior of FeHA towards DOX has been compared to that of synthetic biomimetic apatite (HA) NPs prepared *ad hoc* with characteristics close to those of bone mineral. The DOX adsorption kinetics and isotherms on FeHA and HA were explored and fitted according to different mathematical models (Elovich, Sips and Freundlich) revealing enhanced uptake of DOX on FeHA than HA, due to the better interaction of the drug with the surface iron cations, and because of the formation of multi-molecular DOX assemblies. In the absence of PEMF, the quantity of DOX released from HA was higher than that released from FeHA, in agreement with the lower affinity of DOX for HA than FeHA. Interestingly, in presence of PEMF, the extent of DOX released from FeHA after 3 and 6 days increased significantly. The higher DOX release from FeHA under PEMF can be explained by the mechanical shacking of superparamagnetic FeHA NPs breaking the binding with the drug and allowing detachment of DOX assemblies from NPs surface. In vitro assays demonstrated that DOX loaded on HA and FeHA displayed cytotoxicity against the human osteosarcoma cell line (SAOS-2) at the same level as free DOX, for all the concentrations and time points tested. Confocal microscopy analyses showed that drug-loaded NPs were rapidly internalized within cells and released DOX, which accumulated in the nucleus where it exerted the desired cytotoxic activity.

Key words: nanocrystalline apatite, calcium phosphate, drug delivery, nanomedicine, magnetism

1. Introduction

The use of nanosystems/nanoparticles (that will be described here by the generic abbreviation NPs) as drug carriers has been widely explored during the last 20 years mainly to precisely administer therapeutic molecules in specific parts of the body with the final aim of improving their efficacy (enhancing their concentration at the site of interest and preventing early degradation and clearance) and reducing side effects.[1, 2] Different types of NPs (metallic, inorganic, polymeric, micelles, liposomes, carbon nanotubes, etc.) have been evaluated as drug delivery system particularly in cancer therapy, where serious drug side effects compromise the health of patients.[3, 4]

More recently, the use of magnetic NPs as drug carriers has strongly arisen since they could be manipulated upon application of magnetic fields.[5, 6] In particular, the drug attached to magnetic NPs could be efficiently remotely controlled and targeted in desired areas of the body using external magnetic fields.[7] Moreover, magnetic NPs can also be employed for several other biomedical applications, such as cells label and separation,[8] immunoassay,[9] MRI contrast agents,[10] and hyperthermia.[11] Recently, they were also used to prepare scaffolds for bone tissue engineering.[12, 13] In fact, under magnetic fields, these scaffolds can provide on-demand release of drugs or biomolecules inducing osteogenesis and angiogenesis and at the same time magneto-mechanical stimulation on bone cells favoring proliferation, differentiation and bone healing.[14, 15]

For biomedical applications, a required property of magnetic NPs is the superparamagnetism, which is the ability to be strongly magnetized (i.e., the alignment of all magnetic moments of atoms in parallel along the direction of magnetic field) when they are exposed to low intensity magnetic fields, without having a remnant or residual magnetization when the magnetic fields are removed.[16] This feature is necessary to avoid coagulation and agglomeration of NPs causing possible embolization of capillary vessels when they are used *in vivo*.[17]

So far, magnetic NPs employed for biomedical applications are mainly based on Super-Paramagnetic Iron Oxide Nanoparticles (SPION), consisting in mixtures of magnetite, maghemite and hematite, which have been demonstrated successfully both *in vitro* and *in vivo*.[18] SPION can be synthesized with different morphologies, chemical compositions and magnetic properties but some limitations still exist including low magnetic moment and low cargo capacity.[19] Additionally, although SPION are approved for human *in vivo* use by the American Food and Drug Administration (FDA),[20] several concerns about their cytotoxicity are emerging.[21, 22] In fact, their chronic administration can lead to the accumulation of high quantity

of iron in soft tissues and organs such as liver and kidney, causing an imbalance in their homeostasis and even cytotoxic and inflammatory effects.[23-25]

To overcome the limitations of SPION, new forms of biocompatible superparamagnetic NPs with good magnetic moment, high drug loading capability and lower iron content are strongly required.

Hydroxyapatite (HA), whose stoichiometric composition corresponds to $Ca_{10}(PO_4)_6(OH)_2$, is the most extensively used calcium phosphate phase in several biomedical fields because of its chemical similarity with the mineral phase of bone (composed of nanocrystalline non-stoichiometric carbonated apatites) and thanks to its the well-known properties of biocompatibility, biodegradability and pH-dependent dissolution.[26] HA is mainly employed in bone tissue engineering in the form of scaffolds, injectable cements, coatings for metallic implants and in nanomedicine as NPs in suspension.[26] Whether stoichiometric or not, HA is able to accommodate several substituting ions, while still maintaining its intrinsic structure.[27, 28] In particular, Ca^{2+} ions can be substituted to some extent by monovalent to tetravalent cations (e.g. from Na^{+}, to Zn^{2+}, Fe^{3+} and Ti^{4+}) while PO_4^{3-} can be replaced by divalent (CO_3^{2-}, HPO_4^{2-}), trivalent (AsO_4^{3-}, VO_4^{3-}) and tetravalent (SiO_4^{4-}) anions.[27, 28] Recently Tampieri *et al.*[29] have developed biocompatible and biodegradable ionic substituted-HA NPs endowed with superparamagnetic and hyperthermia features *via* doping HA with Fe^{2+}/Fe^{3+} ions (denoted "FeHA"). Interestingly, even if the iron amount of FeHA NPs is significantly lower than that of maghemite and magnetite NPs, they are featured by comparable superparamagnetic properties and hyperthermia effect.[29] *In vitro* studies have also demonstrated that FeHA NPs (alone or combined with poly(L-lactic) acid or poly(ε-caprolactone)) positively influenced osteoblast-like cells and mesenchymal stem cells viability.[30-32]

The aim of the present work was, in essence, to evaluate the ability of superparamagnetic FeHA NPs to interact with the drug doxorubicin (DOX) (known also as adriamycin) monitoring the drug uptake and then the release over the time both in presence and absence of an applied low-frequency electromagnetic field. DOX is commonly used in chemotherapies due to its therapeutic potential against solid tumors.[33] The chemotherapy based on DOX, however, is limited by dose-dependent cardiotoxic side effects that can potentially lead to heart failure.[33, 34] To avoid this problem, targeted drug delivery could provide therapeutically effective DOX release directly at the tumor site improving the treatment of cancers. Moreover, DOX has strong visible absorption and fluorescence emission, therefore is one of the best molecule for pursuing the objective of this study, since its uptake and release from NPs can be easily monitored.[35]

The behavior of FeHA towards DOX has been compared to that of an iron-free biomimetic apatite nanocrystals prepared ad "hoc" with characteristics very close to those of bone mineral (denoted HA). This latter material, which has already demonstrated high ability to bind and release several types of drugs such as tetracycline and bisphosphonates,[36, 37] can be viewed as a biomimetic "golden synthetic standard" for bone mineral. The adsorption of bioactive molecules on the surface of biomimetic apatite (as opposed to simple impregnation) allows the formation of stable bindings with the nano-carrier. These properties were attributed to the existence of a hydrated layer at the surface of the biomimetic apatite nanocrystals containing mobile ions with a higher reactivity than those present at the surface of well-crystallized apatite. It thus allows a better control of the dose of the drug released, with a slowed delivery, for localized tailored therapeutic applications.[38] Finally, the cellular uptake and cytotoxic activity of DOX-loaded FeHA and HA NPs were analyzed, as a proof of concept, *in vitro* in human osteosarcoma (SAOS-2) cell line.

2. Materials and methods

2.1 Materials

Ammonium phosphate dibasic ($(NH_4)_2HPO_4$, ACS reagent), calcium hydroxide ($Ca(OH)_2$, ACS reagent), calcium nitrate tetrahydrate ($Ca(NO_3)\cdot 4H_2O$, BioXtra), dimethyl sulfoxide (DMSO, $(CH_3)_2SO$, for molecular biology), doxorubicin hydrochloride ($C_{27}H_{29}NO_{11}\cdot HCl$, DOX, European Pharmacopoeia (EP) Reference Standard), HEPES sodium salt ($C_8H_{17}N_2NaO_4S$, BioXtra), iron(II) chloride tetrahydrate ($FeCl_2\cdot 4H_2O$, ReagentPlus®), iron(III) chloride hexahydrate ($FeCl_3\cdot 6H_2O$, ACS reagent), isopropyl alcohol ($(CH_3)_2CHOH$, ≥99.7%, FCC, FG), phosphoric acid (H_3PO_4, ≥85 wt% in H_2O), nitric acid (HNO_3, ACS reagent, 70%), potassium chloride (KCl, BioXtra) and sodium bicarbonate ($NaHCO_3$, ACS reagent), thiazolyl blue tetrazolium bromide (MTT, $C_{18}H_{16}BrN_5S$, BioReagent), trypan blue ($C_{34}H_{24}N_6O_{14}S_4Na_4$, BioReagent) were purchased from Sigma-Aldrich and used as-received without any further purification. Dulbecco's modified eagle medium (DMEM F12), fetal bovine serum (FBS), Dulbecco's phosphate buffered saline (DPBS) without calcium and magnesium, penicillin–streptomycin, trypsin–EDTA, and 4,6-Diamidino-2-phenylindole dihydrochloride (DAPI) were purchased from Invitrogen Corporation (Carlsbad, USA) and used as-received without any further purification. Human Osteosarcoma cell line SAOS-2 was purchased from ATCC (Manassas, USA). Ultrapure water (0.22 µS, 25 °C, Milli-Q, Millipore) was used in all of the experiments.

2.1 Synthesis of superparamagnetic iron-substituted nanocrystalline apatite (FeHA)

Superparamagnetic iron-substituted apatite (which will be referred to as "FeHA" in this study) was synthesized according to the method developed by Tampieri *et al.*[29] Briefly, an aqueous solution of H_3PO_4 (44.4 g in 300 mL) was dropped into an aqueous suspension of $Ca(OH)_2$ (50.0 g in 400 mL) containing $FeCl_2 \cdot 4H_2O$ (12.7 g) and $FeCl_3 \cdot 6H_2O$ (17.9 g) as sources of Fe^{2+} and Fe^{3+} ions, respectively, under constant heating and stirring at 40°C. Once the neutralization reaction was completed, the solution was kept in the same conditions used during the neutralization reaction for 1 h, and then left to age for 24 h at room temperature without further stirring. The precipitate was separated from the mother liquor by centrifugation, washed three times with water by centrifugation and freeze-dried. The powder was then sieved (< 125 μm) and stored in a freezer prior to use.

2.2 Preparation of iron-free biomimetic nanocrystalline apatite (HA)

The iron-free nanocrystalline apatite powder (which will be referred to as "HA" in this study) was prepared by double decomposition technique at ambient temperature and close-to-physiological pH (7.47) by pouring an aqueous solution of $Ca(NO_3) \cdot 4H_2O$ (52.2 g in 750 mL) into a carbonate and phosphate aqueous solution (165.8 g of $(NH_4)_2HPO_4$ and 9.0 g of $NaHCO_3$ in 1500 mL). The precipitate obtained was left to mature for one day at 50°C, filtered, washed three times with deionized water and freeze-dried. The powder was then sieved (< 125 μm) and stored in a freezer prior to use.

2.3 Characterization of HA and FeHA

The X-ray diffraction (XRD) patterns of the samples were recorded with a D8 Advance Diffractometer (Bruker, Karlsruhe, Germany) equipped with a Lynx-eye position sensitive detector using Cu Kα radiation (λ = 1.54178 Å) generated at 40 kV and 40 mA. XRD spectra were recorded in the 2θ range from 10 to 60° with a step size (2θ) of 0.02° and a counting time of 0.5 s. The crystallite sizes of HA and FeHA along the *c*-axis and along perpendicular direction were estimated by applying Scherrer's formula[39] using the 2θ=25.8° and 2θ=39.7° diffraction peaks, corresponding to the (002) and (310) reflections, respectively.

Fourier transform infrared (FTIR) spectroscopy analyses were achieved on a Nicolet 5700 spectrometer (Thermo Fisher Scientific Inc., Waltham, USA) with a resolution of 4 cm^{-1} by accumulation of 64 scans covering the 4000 to 400 cm^{-1} range, using the KBr pellet method.

Calcium, phosphate and iron contents were determined by inductively coupled plasma optical emission spectrometry (ICP-OES) with a Liberty 200 spectrometer (Varian, Palo Alto, USA). An aliquot of 20 mg of sample was dissolved in 50 mL of a 1 wt % HNO_3 solution prior the analysis.

Carbonate titration was carried out by coulometry using a CM 5014 coulometer with CM 5130 acidification unit (UIC Inc., Joliet, USA). All chemical titrations were associated to a relative error of about 1%. A BELSORP mini II apparatus (Microtrac, Krefeld, Germany)) (BET method based on nitrogen adsorption) was used to determine the specific surface area (SSA_{BET}) of the samples.

Size and ζ-potential were measured by dynamic light scattering (DLS) with a Zetasizer Nano ZS (Malvern, Worcestershire, UK). NPs were suspended in 0.01 M HEPES buffer at pH 7.4 at a concentration of 0.1 mg mL^{-1}. For size distribution measurements, low-volume quartz cuvettes (Hellma, Müllheim, Germany) were used. Ten runs of 30 s were performed for each measurement and four measurements were carried out for each sample. To evaluate the stability of apatite NPs and of the corresponding DOX adducts in suspension, derived count rate (cps) were recorded continuously for 60 min. ζ-potential was quantified by laser doppler velocimetry as electrophoretic mobility using disposable electrophoretic cells (Malvern, Worcestershire, UK). Twenty runs of 3 s were collected in each measurement.

Transmission Electron Microscopy (TEM) observations were performed using a Tecnai F20 (FEI, Hillsboro, USA) equipped with a Schottky emitter and operating at 120 keV. The instrument was also equipped with an Energy Dispersive X-Ray Spectrometer (EDX) for X-Ray microanalysis on selected areas. The powder samples were dispersed in isopropyl alcohol, treated with ultrasounds and then a few droplets of the slurry were deposited on holey-carbon foils supported on conventional copper microgrid (300 mesh).

2.4 Drug adsorption and release experiments

DOX adsorption experiments on apatitic substrates (HA and FeHA) were carried out using a constant solid-to-solution ratio corresponding to 20 mg of apatite in 5 mL of DOX solution at increasing concentrations (0.1-5.0 mg mL^{-1}). The amount of DOX adsorbed (Q_{ads}) for any data-point was determined by comparing the amount of DOX remaining in solution after the adsorption experiment (supernatant) to the initial concentration; DOX being directly titrated by visible spectrophotometry (absorption at λ=496 nm) using a Cary Bio spectrophotometer (Varian, Palo Alto, USA). KCl 0.01 M was used as solvent in all experiments to provide nearly

constant ionic strength. A calibration curve (linear correlation factor of 0.9998) was previously drawn for standard solutions of DOX concentrations ranging from 0.001 to 0.025 mg mL^{-1}.

Adsorption experiments were carried out at 37 °C, placing vials in horizontal setting to ensure an optimal interaction between the surface of the apatite substrates and the solution. After the contact time determined in a preliminary step (see text), the system was centrifuged (5000 rpm for 5 min) to allow retrieval of the solid and sampling of the supernatant for quantification of DOX.

HA and FeHA functionalized with the maximum loading amount of DOX were analyzed by Raman micro-spectrometry, Cross Polarization Magic Angle Spinning (CP/MAS) solid-state nuclear magnetic resonance (NMR), FTIR and DLS.

Raman analyses were carried out on a confocal Labram HR800 micro-spectrometer, typically making observations in the range 400-4000 cm^{-1}. The samples were exposed in backscattering mode to 633 nm He/Ne laser. Measurements were carried out with a spectral resolution of 3 cm^{-1}. An optical objective x100 was used, conferring to the system a lateral resolution of 0.7 μm and an axial resolution of 2.7 μm.

Solid-state Cross-Polarization Magic Angle Spinning Carbon-13 Nuclear Magnetic Resonance experiments (CP/MAS -NMR) were performed on a Bruker Avance III 400 WB spectrometer operated at 9.4 T, 400 MHz, with V_r=10 kHz (probe 3.2 mm), and an accumulation performed overnight. ^{13}C chemical shifts were externally referenced to tetramethylsilane (TMS).

FTIR and DLS analysis on the DOX loaded NPs were carried out as reported above for the un-functionalized NPs.

DOX release experiments from HA and FeHA (previously functionalized with maximum loading amount of DOX) were carried out at 37°C in the presence or absence of pulsed electromagnetic fields (PEMF). Investigations in the presence of PEMF were achieved placing the powder samples in an home-made device similar to that previously developed by Fassina et al.[40] (Figure S1, ESI). Briefly, it consisted of a windowed polymethylmethacrylate tube carrying a well-plate containing the samples and two solenoids (i.e., Helmoltz coils, the planes of which were parallel). The generated magnetic field and the induced electric field were perpendicular and parallel to the samples, respectively. Samples were 5 cm distant from each solenoid plane, and a Biostim SPT pulse generator (Igea, Carpi, Italy) was used to power the solenoids. According to position of the solenoids and the characteristics of the pulse generator, the electromagnetic stimulus had the following parameters: intensity of the magnetic field equal to 2.0 ± 0.2 mT, amplitude of the induced electric tension equal to 5 ± 1 mV, frequency of 75 ± 2 Hz, and pulse duration of 1.3 ms. Samples were prepared using a constant solid-to-solution ratio

corresponding to 5 mg of drug-apatite conjugate in 2.5 mL of HEPES buffer at pH 7.4 (0.01 M HEPES, 0.01 M KCl). At the scheduled times ranging from 1 to 6 days, the temperature of the samples were measured (only those exposed to PEMF), centrifuged (5000 rpm for 5 min) to allow retrieval of the solid and sampling of the supernatant for quantification of DOX. The amount of DOX in the medium was determined by visible spectrophotometry as reported above. Dissolution of HA and FeHA in presence and in absence of PEMF (using the same apparatus described above) was evaluated adding 10 mg of apatite in 10 mL of HEPES buffer at pH 7.4 (0.01 M HEPES, 0.01 M KCl). At scheduled times (up to 7 days), the supernatant (that was well separated from the solid phase by centrifugation) was removed, centrifuged and filtered at 0.25 μm in view of Ca^{2+} quantification by ICP-OES.

2.5 In vitro cell culture

Human Osteosarcoma cell line SAOS-2 was cultured in DMEM F12, 10% FBS and 100 U mL^{-1} penicillin/streptomycin and kept at 37°C in an atmosphere of 5% CO_2. Cells were detached from culture flasks by trypsinization, centrifuged and re-suspended. Cell number and viability were assessed with the trypan-blue dye exclusion test. For the experiments, the cells were plated at a density of 5×10^3 cells/well in 96-well plates, 24 hours after seeding the samples were added to the culture and the cells were maintained in cultured for 24, 48 and 72 hours. HA and FeHA loaded with similar amount of DOX (475 and 449 μg of DOX on 1 mg of HA and FeHA, respectively) were added to the culture at 10 and 100 μM concentration of attached DOX (Table S1, ESI). Moreover, the equivalent amounts of un-functionalized HA and FeHA NPs used for each samples and free DOX were tested (Table S1, ESI). A group of cells only was used as control group. Cells were incubated under standard conditions (37°C, 5% CO_2). All cell-handling procedures were performed in a sterile laminar flow hood.

2.6 Cell viability evaluation

The MTT reagent was prepared at 5 mg mL^{-1} in 0.01M PBS. Cells were incubated with the MTT reagent 1:10 for 2 h at 37°C. Medium was collected and cells incubated with 1 mL of DMSO for 15 min. In this assay, the metabolically active cells react with the tetrazolium salt in the MTT reagent to produce a formazan dye that can be observed at absorbance max of 570 nm, using a Multiskan FC Microplate Photometer (Thermo Scientific, Waltham, USA). This absorbance is directly proportional to the number of metabolically active cells. Mean values of absorbance were determined. The samples of three different experiments were analyzed in triplicate.

2.7 NPs-DOX uptake and nuclear-localization

After 24 hours, cells were washed twice with 0.01 M PBS for 5 min, fixed with 4% (w/v) paraformaldehyde for 15 min, washed with 0.01 M PBS for 5 min and incubated with DAPI for 7 min. Images were acquired by Inverted Ti-E fluorescence microscope (Nikon, Chiyoda, Japan). One representative field of each sample and the co-localization of the nuclear marker, DAPI, and DOX were analyzed.

2.8 Statistical analysis

Experiments were carried out in triplicate and results were expressed as mean and standard error of the mean (SEM). Analysis of cell viability was made by two-way analysis of variance (ANOVA), followed by Bonferroni's post hoc test. Statistical analyses were performed by the GraphPad Prism software (version 5.0), with statistical significance set at $p \leq 0.05$.

3. Results and discussion

3.1 Chemical-physical and morphological characteristics of FeHA and HA

FeHA NPs exhibiting a saturation magnetization of 4.00 ± 0.01 Am^2 Kg^{-1} and endowed with hyperthermia feature (temperature increase of about 40°C in 60 s under an alternating magnetic field of 0.03 N A^{-1} m^{-1} at a frequency of 293 kHz) were synthesized according to the procedure reported by Tampieri *et al.*[29] Iron-free biomimetic HA NPs were synthesized *ad hoc* to possess chemical-physical features (i.e. crystallinity degree, chemical composition, carbonate extent and morphology) similar to those of biogenic bone apatites. An adequate amount of carbonate species (employing $NaHCO_3$) were added in the reaction medium to synthesize HA with similar carbonate extent to that present in bone apatite (3-6 wt%).[26] Carbonate was included during the preparation of HA also as a strategy to favor the formation of small NPs with low crystallinity degree since carbonate ions are well-known inhibitors of apatite crystal growth and its incorporation leads to a reduction of the crystalline order and dimensions.[41, 42]

Both FeHA and HA exhibited similar XRD patterns, with broad and poorly defined peaks (which can be indexed according to the crystallographic features of hydroxyapatite, JCPDS no. 09-432) which is characteristic of bone nanocrystalline apatite (Figure 1A).[43] The presence of the peak at 35.4° (corresponding to (311) plane of Fe_3O_4; JCPDS no. 00-003-0863) in the XRD pattern of FeHA established the presence of a small amount of magnetite (2.6 ± 0.2 wt%)[29] (Figure 1A). The mean crystallite sizes of FeHA and HA (Table 1), calculated along the (002)

and (310) directions applying the Scherrer's formula, evidenced that both samples had the same crystallite dimension along the plane perpendicular to the *c*-axis, while FeHA was composed of more elongated crystallites along the *c*-axis with higher aspect ratio than HA. The lower aspect ratio (i.e. more isometric particles) of HA compared to FeHA was ascribed to the higher presence of carbonate ions inside the crystal lattice as already reported.[42, 44]

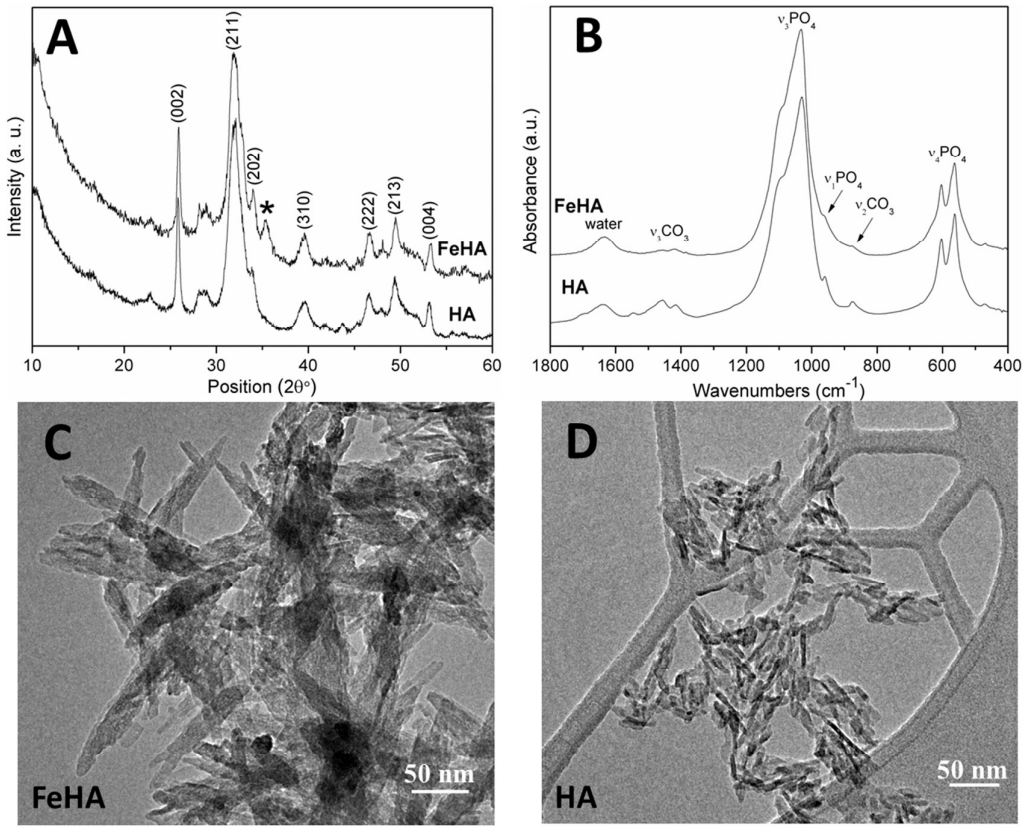

Figure 1. (A) XRD spectra, (B) FTIR spectra and (C-D) TEM images of FeHA and HA NPs.

FTIR spectra of HA and FeHA revealed the typical bands of poorly crystalline biomimetic apatite (i.e. PO_4^{3-} vibration bands at ca. 560−603 (ν_4), 962 (ν_1), and 1000−1104 cm^{-1} (ν_3))[45] (Figure 1B). Bands at 870 (ν_2), 1420 and 1470 cm^{-1} (ν_3) assignable to CO_3^{2-} vibrations characteristic of mostly B-type carbonate-apatite (i.e., CO_3^{2-} replacing PO_4^{3-})[45] were also present in both samples. The bands assigned to CO_3^{2-} were more intense in the case of HA as a more limited amount of carbonate, derived from the atmospheric CO_2, was adsorbed on the surface and/or entrapped in the lattice of FeHA during the synthesis. The carbonate extent in the FeHA and HA was quantified to be 3.0±0.1 and 1.5±0.1 wt%, respectively (Table 1). The Ca/P ratio of FeHA was remarkably lower (1.41±0.03) compared to that of stoichiometric hydroxyapatite

(1.67) because of a partial substitution of Fe^{2+} and Fe^{3+} for Ca^{2+} ions. The Ca/P ratio of HA was also noticeably lower (1.34), pointing to the non-stoichiometry of this compound and its similarity with bone apatite.[26]

Table 1. Bulk Ca/P molar ratio, carbonate extent, mean crystallite sizes along *c* and *ab*-axes (L_{002} and L_{310}, respectively), specific surface area (SSA_{BET}), ζ-potential and mean hydrodynamic radius (R_H) of FeHA and HA NPs.

Sample	Ca/P ratio	CO_3 (%wt)	L_{002} (nm)	L_{310} (nm)	SSA_{BET} (m^2g^{-1})	ζ-potential (mV)	R_H (nm)
FeHA	1.41±0.03	1.5±0.1	18±3	15±3	44±1	-17.6±1.0	120±2
HA	1.34±0.02	3.0±0.1	31±5	18±3	102±1	-18.2±1.3	74±1

TEM images of FeHA showed needle-like crystals, rather heterogeneous in size, having dimensions of 10-30 nm in width and 70-100 nm in length mainly composed of smaller aggregated and isometric NPs of about 5-10 nm in width and 10-20 nm in length (Figure 1C). A very low concentration of dark spots (5–10 nm in size), corresponding to inclusions of Fe-rich phases as demonstrated by EDX analysis, was also visible. EDX elementary analysis carried out in selected area of FeHA sample containing and not containing the dark spots, revealed that the amount of iron in the area rich of black spots is much higher than that in the part without dark spots (Figure S3, ESI). TEM images of HA displayed elongated NPs having dimensions of 5-10 nm in width and 20-30 nm in length (Figure 1D). HA NPs were less aggregated than FeHA presenting a higher specific surface area (SSA_{BET}) (Table 1). The higher tendency of FeHA to form aggregates respect to HA was ascribed to the greater amount of foreign ions (i.e. Fe^{2+}, Fe^{3+}, CO_3^{2-}) causing crystal lattice distortion, reduction of the long-range periodic regularity, and possible modifications of surface energy.[46] The higher structural disorder can induce the formation of quasi-amorphous parts, especially at the surface, causing junction and adhesion of crystals by inter-crystalline interactions during the synthesis or post synthesis under drying. The similar surface negative charge of FeHA and HA at pH 7.4 (Table 1) was attributed to the existence of a hydrated surface layer (which is a peculiar feature of bone apatite and its biomimetic counterpart) composed of disordered Ca^{2+}, PO_4^{3-} and HPO_4^{2-} ionic groups in non-apatitic structural environments, having an impact on the surface charge of the nanocrystals.[47] However, it is worthwhile to mention that ζ-potential measurements only estimate the net surface charge of NPs, thus even if a negative value is recorded, this does not imply that only negatively charged sites are present on the NPs surface. The mean hydrodynamic radius (R_H),

calculated by DLS, of FeHA was larger than HA (Table 1) in agreement with the higher tendency of FeHA to form aggregates.

The higher sizes determined by DLS in comparison to those quantified by TEM were consistent with the fact that TEM provides information on individual NPs and the sample is dehydrated and immobilized on a solid support, in contrast DLS gives the average of the hydrodynamic size of an ensemble of dispersed NPs.[48]

All the chemical-physical characteristics of the apatitic NPs reported above highlighted the biomimetic features of HA thanks to the evident morphological and structural similarities with bone apatite. FeHA NPs were primarily different respect to HA in terms of chemical structure, surface area and tendency to form aggregates, while they had comparable surface charge and morphology.

3.2 Adsorption of DOX on HA and FeHA

The adsorption study was organized in two steps aiming, firstly, at inspecting the kinetics of adsorption, and secondly, at determining the adsorption isotherms (at 37°C).

In a first stage, the adsorption kinetics of DOX on HA and FeHA substrates were investigated. The kinetic overview was made possible by following the amount of DOX adsorbed (Q_{ads}) as a function of contact time between the inorganic substrate and the drug. The evolution of Q_{ads} (given in μmol DOX/m² apatite) versus time is plotted on Figure 2 in the case of a constant DOX concentration of *ca.* 5 mmol L^{-1}.

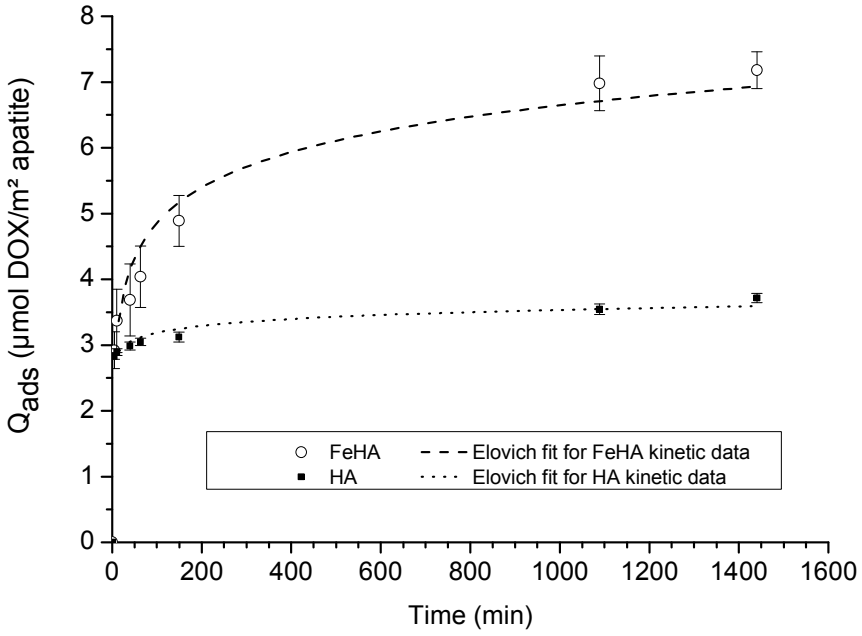

Figure 2. Adsorption kinetics of DOX on (○) FeHA and (■) HA NPs. Separate points are the experimental data; dotted lines indicate Elovich fits of kinetic data.

These data indicated that in both cases the adsorbed amount increased as a function of time, although in different ranges, with a first rapid rise followed by a progressive stabilization: up to around 3.5 µmol DOX/m² apatite (~2 mg/m²) in the case of HA compared to a two-fold value of *ca*. 7 µmol/m² (~4 mg/m²) for FeHA. The shape of these kinetic curves points to a rather rapid adsorption of the DOX molecules, although faster for HA (around 200 min) than for FeHA (around 1000 min). The data have been tentatively fitted to the kinetic models often encountered, namely the pseudo-first-order and pseudo-second-order as well as a general kinetic law of order "n", and finally to the Elovich model, in a similar way as was done recently in the study of tetracycline adsorption on biomimetic apatite.[36] Only the latter led to satisfactory correlation coefficients (R^2 greater than 0.97) with respectively $R^2 = 0.9766$ for FeHA and 0.9945 for HA. In contrast, kinetic models of order "n" (including with n = 1 and n = 2) led to uncorrelated data showing that the adsorption kinetics followed a more complex process. A relatively good fit (see dotted lines in Figure 2) to the Elovich model, a logarithmic function of time, is often encountered for the adsorption of polyelectrolytes on heterogeneous surfaces.[49, 50]

The molecular structure of DOX is represented in Figure S2, ESI. It is composed of an (aromatic) anthracycline ring linked to an amino-sugar: the pK value of the amino group was

reported around 8.2,[51, 52] while other pK values of the molecule (typically for –OH groups) were found beyond 9.5. This indicates that, in physiological conditions, the DOX molecule exists mainly in its acidic form, that is with a protonated amino group. The multiple oxygen atoms of the molecule offer on the other hand many polar groups (especially thanks to the conjugation of several double bonds and non-bonding doublets), but the hydrogen atoms linked to the –OH groups of the molecule are expected to remain present at physiological pH (7.4). This leads to a situation where the DOX molecule exposes an $-NH_3^+$ group and several oxygens providing multiple potential "interaction points" with apatite nanocrystals, despite the lack of anionic end-groups with well-known high affinity for apatitic surfaces such as phosphate, phosphonate or even carboxylate.[53, 54] This multiplicity of interaction sites on the DOX molecule may explain, in conjunction with the relative heterogeneity of the substrates, the relatively good fit with the Elovich equation and the absence of any satisfying correlation with other kinetic models.

The modeling of adsorption data over a long period of time however poses the potential issue of progressive modifications of non-stoichiometric apatitic substrates, which can further mature or else undergo dissolution or partial re-precipitation phenomena. In this study, we selected as contact time for the adsorption isotherms the value of 90 min to limit significant post-maturation effect in the solids and dissolution.

In a second stage, using this selected contact time, the adsorption isotherms of DOX on both FeHA and HA have been analyzed by performing experiments with increasing DOX concentrations. Figure 3 reports the obtained isotherms (at 37°C in KCl 10^{-2} M) for Q_{ads} expressed in µmol DOX/m² apatite and C_{eq} (the equilibrium concentration reached) in mmol/l. Interestingly, these two isotherms were found to exhibit distinct shapes. The different mechanism of adsorption observed can reasonably be attributed to the presence of iron within the apatite lattice as well as the small amount of a secondary iron oxide phase in the FeHA sample, thus leading to different types of accessible surface sites.

In the case of the iron-free HA substrate, the isotherm curve showed a first steep increase of the amount of DOX adsorbed for equilibrium concentration of up to C_{eq}~1 mmol L^{-1}, followed by a stabilization for greater concentrations. This general tendency points to an adsorption behavior with a progressive filling of surface sites and towards a maximal degree of coverage. This type of evolution is noticed in particular for the Langmuir model and for the more general equation of Sips (Langmuir-Freundlich):

$$Q_{ads} = Q_m \cdot \frac{K_S \cdot C_{eq}{}^m}{1 + K_S \cdot C_{eq}{}^m} \qquad \text{Sips isotherm}$$

which comes back to the Langmuir model for the particular case of $m = 1$. In this equation, Q_m designates the maximal adsorption coverage, C_{eq} is the equilibrium DOX concentration for the considered data-points, "*m*" is the Sips exponent, and K_S is the Sips constant.

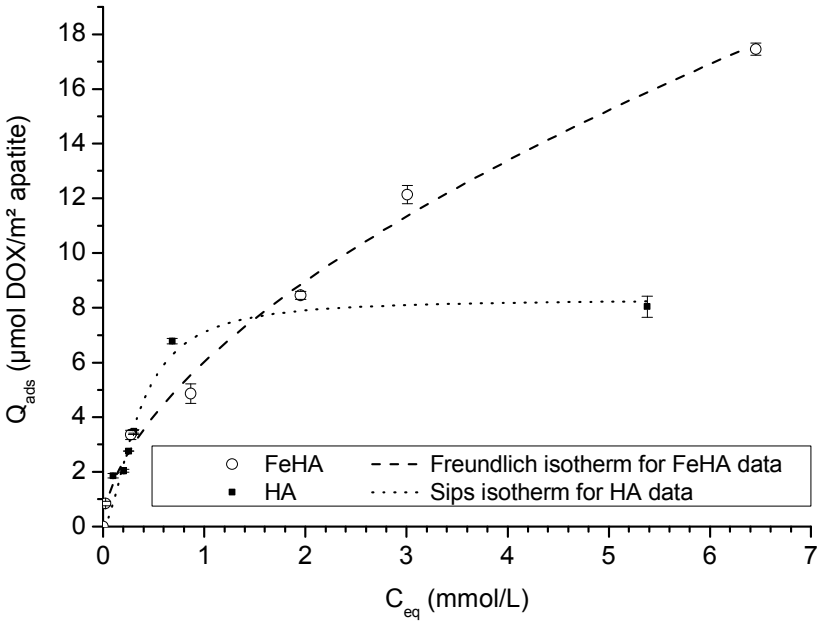

Figure 3. Adsorption isotherms of DOX on FeHA (○) and HA (■). Separate points are the experimental data; dotted lines indicate Freundlich and Sips fits of isotherm data for FeHA and HA, respectively.

A mathematical analysis indicates that the adsorption data for the system HA-DOX can best be fitted with the Sips model ($R^2 = 0.9703$) with $K_S = 5.96 \pm 3.27$ and $m = 1.7 \pm 0.4$. Despite a non-negligible uncertainty, the value of "*m*" appears noticeably distinct from unity, thus suggesting a neat departure from the standard Langmuirian case. A value of "*m*" greater than 1 can suggest the existence of significant positive interactions (molecular cooperativity) of adsorbed molecules among each other.[55, 56] This situation was recently also encountered for the adsorption of other biomolecules on biomimetic apatites, such as tetracycline[36] and cytidine monophosphate,[57] but the maximal adsorbed amounts for these two other molecules were significantly lower than the one observed here. As in the case of tetracycline, DOX molecules do not expose high-affinity end-groups for the surface of apatite; the amount of DOX adsorbed on HA is however found particularly high, reaching ~8 µmol DOX/m² apatite. It suggests a rather high affinity of DOX for apatitic substrates, in agreement with a preliminary work indicating the value 8.2 µmol/m²,[58] but in contrast to what could have been expected from such molecules without specific high-

affinity end-groups for apatite surfaces. The range of adsorbed quantities can be compared to other adsorption data obtained for rather similar conditions/substrates. For example, the maximal adsorbed amount reached *ca.* 2.7 µmol/m² for the adsorption of tiludronate (an anti-osteoporotic bisphosphonate compound) on carbonated nanocrystalline apatite,[37, 59] or else ~2.4 µmol/m² for platinum bisphosphonate complexes.[60] The observation of a high affinity of DOX for the apatitic surface is surprising taking into account the absence of known high-affinity anionic end-groups such as phosphates, phosphonates or carboxylates, and also in comparison with the adsorption of tetracycline which led to a maximal coverage of 0.66 µmol/m² (on a carbonated apatite matured for 1 week at room temperature).[36] DOX molecules are expected to interact with apatite surfaces mostly through its multiple polar sites, but these sites are also susceptible to allow interactions among neighboring DOX molecules for a cooperative adsorption, as already suggested by the value of the Sips parameter "*m*".

DOX molecules however present an important peculiarity over other molecules tested so far in adsorption experiments involving apatites: this water-soluble molecule is indeed composed of a large hydrophobic anthracycline ring composed of 4 coplanar carbon cycles (see Figure S2, ESI), attached to a smaller hydrophilic side chain. In this context, hydrophobic/hydrophilic properties are expected to significantly affect the behavior of DOX molecules in aqueous-based experiments.[61] The presence of this large planar aromatic portion of the molecule is at the origin of the therapeutic activity of DOX via intercalation within DNA strands. Several studies have pointed out the possibility for DOX molecules to self-assemble, forming dimers, trimers or even much larger polymolecular units.[52, 61, 62] This type of molecular interaction between DOX molecules is believed to involve π-π stacking processes of their coplanar aromatic domains;[61] and both parallel and antiparallel stacking can be considered between interacting DOX molecules.[62] Such strong molecular interactions/stacking (dictated by optimal spatial distribution of hydrophobic and hydrophilic parts of the molecules) are also likely to occur in an adsorption context, where the molecules are contacted not only with an aqueous solution but also with a solid surface. This phenomenon could indeed explain the exceptionally high adsorbed amounts noticed for the HA-DOX system as compared to the case of other organic molecules: instead of having only individual "monomeric" DOX molecules adsorbed on the apatitic surface, strongly-interacting molecules could organize in a stable manner on the surface of the solid and among each other, leading to what could be finally considered as a "high affinity" system with favored basal and lateral interactions. The fact that the HA-DOX isotherm reaches a stabilized plateau indicates that the adsorption process finally leads to a DOX-saturated surface where no further

molecules can be added (at this temperature), and the relatively good fit to the Sips model suggests that, at least macroscopically, the adsorption process can be satisfyingly treated by considering the adsorption of initially monomeric DOX with significant cooperativity between adsorbed DOX molecules (although the exact orientation and positioning of the species cannot be categorized at this point).

The Sips affinity constant K_S (recalculated for C_{eq} expressed in mol/L) is itself related to the standard Gibbs free energy ($\Delta G_{ads}°$) of the global adsorption process by the relation:

$$K_S = \exp\left(-\frac{\Delta G_{ads}°}{RT}\right)$$

When applied to the present HA-DOX system, this equation leads to $\Delta G_{ads}° \cong -35$ kJ mol^{-1}. Although this value relates to standard conditions, it allows comparisons with the same property for other adsorption systems. It is in particular more negative than the $\Delta G_{ads}°$ values estimated for the systems tetracycline/apatite[36] and cytidine monophosphate/apatite[57] (of the order of -20 kJ mol^{-1}), indicating a more energetically favorable process. These findings are in agreement with the above experimental results and discussion, pointing out high adsorbed amounts and strongly suggesting the existence of interactions between DOX molecules.

In the case of the FeHA, even greater adsorbed amounts were observed as compared to HA, and the shapes of both isotherms were significantly different (Figure 3). When expressed in µmol/m², the adsorbed amounts reached for FeHA appear somewhat lower than the values obtained for HA only up to an equilibrium concentration of *ca.* 1.5 mmol L^{-1}; beyond this concentration limit, the adsorbed amount continues however to increase without stabilizing in the rather large concentration window 1.5–7 mmol L^{-1}. The values of N_{ads} reached here (up to 18 µmol/m² when expressed per unit surface area) are particularly high for apatitic surfaces and especially in comparison to the adsorption data obtained previously on the HA substrate. In both cases (FeHA and HA), the formation of multi-molecular DOX assemblies adsorbed has to be considered to explain these observations, as was developed above for the system HA-DOX, but the significant further increase observed for FeHA can only be assigned to the presence of iron doping (as iron-substituted apatite but also as small percentage of iron oxide secondary phases, see Fig. 1), thus providing additional adsorption sites. In solution, the presence of divalent and trivalent ions was shown to favor the interaction among DOX molecules towards the formation of multimolecular self-assemblies, and the case of Fe^{3+} was particularly noticed:[61] quelamycin (triferric doxorubicin) is a derivative of DOX exploiting this specificity of iron-DOX

interaction.[63-65] The good affinity of DOX for iron cations is thus likely to take a large part in the greater adsorbed amount noticed for FeHA-DOX in comparison to HA-DOX.

The mathematical modeling of the FeHA-DOX adsorption isotherm is delicate because various types of adsorption sites coexist, in the form of separate crystalline phases. The overall adsorption process is thus composed of a superimposition of various adsorption phenomena involving the various types of surface sites accessible to DOX molecules. In this context, the global isotherm corresponds to a sum of events and should only be seen as a "macroscopic" result. However, being able to describe it mathematically could prove useful, from a practical viewpoint, for example for being able to estimate the amount of DOX molecules susceptible to adsorb on such a substrate in a given concentration scenario. Application of the Sips model did not allow here a good description of the FeHA-DOX data without very large uncertainties on Sips parameters. This can be related to the coexistence on this sample of different crystalline phases with distinct adsorptive behaviors. The mathematical modeling of the global FeHA-DOX isotherm using Freundlich's equation ($Q_{ads} = K_F \cdot C_{eq}^{1/n}$) led, on the contrary, to a satisfying overall fit, with a value of "n" of 1.7±0.1 and a correlation coefficient of $R^2 = 0.9919$. Freundlich's model has initially been established for explaining adsorption data on non-equivalent adsorption sites corresponding to a range of adsorption energies (rather than a constant value as is the case in Langmuir's theory). The goodness of fit noticed here with the Freundlich model probably arises from the existence, in the FeHA substrate, of a series of adsorption sites with a non-negligible span in energy. Even if it is not possible at this stage to give more detail on the type of interaction existing between the multi-phased FeHA sample and DOX nor between adjacent DOX molecules, this mathematical modelling at least allows one to satisfyingly describe the overall evolution of Q_{ads} versus C_{eq}.

3.3 Characterization of HA and FeHA functionalized with DOX

In order to get more information on the interaction mechanism of DOX with HA and FeHA and to evaluate how the functionalization can affect the surface properties and the size of the NPs, the ζ-potential and the mean R_H of the HA and FeHA functionalized with the maximum amount of DOX were measured. The coupling of HA and FeHA with DOX altered their surface charge, in particular this functionalization caused a shift of the ζ-potential of HA and FeHA (-5.6±2.0 and -8.1±3.5 mV, respectively) toward less negative values. This finding is in agreement with a possible interaction of the positively charged $-NH_3^+$ groups of the DOX dimers with the negatively charged surface groups of apatites (i.e. phosphate, phosphonate or even carboxylate)

as reported above. The surface uptake of DOX provided the NPs with less negative surface charge, which in turn also decreased the inter-particles repulsion. Consequently, HA-DOX and FeHA-DOX were more aggregated, forming less stable suspension than the bare ones with increased mean R_H of 281 ± 24 and 354 ± 52 nm, respectively. The stability in an aqueous suspension of bare and functionalized NPs (0.1 mg mL^{-1}) as a function of time has been evaluated by DLS, measuring continuously for 60 min the derived count rate (Figure S4, ESI). In the case of HA and FeHA the recorded values remained nearly constant, corroborating that neither a significant aggregation nor a fast sedimentation occurred. On the contrary, in the case of functionalized NPs the fast drop of the derived count rate revealed their lower stability in suspension.

Comparison of the FTIR spectra of FeHA-DOX, HA-DOX and free DOX (Figure S5, ESI) was not useful to shed some light on the interaction mechanisms of DOX molecules with the inorganic phase. Nevertheless, the appearance of DOX main signal at 1284 cm^{-1} (C–O–C asymmetric stretching[66]) in the spectra of FeHA-DOX and HA-DOX confirmed the effective uptake of the drug on the NPs.

Raman microanalyses were run on the solids after adsorption, but no useable data on the position of bands and eventual shifts were obtained due to strong fluorescence artifacts from DOX with the employed laser wavelength at our disposal (Figure S6, ESI). Moroever, ^{13}C CP/MAS solid-state NMR analyses were tentatively run to observe the interaction of DOX molecules with the surface of apatite nanocrystals. However, although the recorded signals can be well correlated to the presence of DOX (Figure S7, ESI), they only showed a low-intensity noisy signal not exploitable for drawing conclusive statements on the chemical interaction of the drug with the apatitic substrate, which can be linked to the limited amount of DOX on the samples and to the low isotopic abundance of ^{13}C.

3.4 Release of DOX from HA and FeHA

HA and FeHA were functionalized with similar amounts of DOX (i.e. 475 and 449 μg of DOX on 1 mg of HA and FeHA, respectively) corresponding to the maximum drug loading capacity of HA. The DOX release efficacy (D_R) from drug-loaded HA and FeHA, defined as the ratio (%wt) between the amount of drug released at different times ($Q_{(t)}$) and the initial drug loading capacity Q_i, was calculated by the following formula:

$$D_R = \frac{Q_{(t)}}{Q_i} \times 100$$

D_R of DOX from HA and FeHA as a function of time in close to physiological conditions (pH 7.4) without and in the presence of PEMF is shown in Figure 4. In the absence of PEMF, the percentage of DOX released from HA was higher than that released from FeHA. DOX was gradually released from HA as a function of time reaching after 6 days the value of about 15wt% of the initial DOX loaded. On the contrary, the maximum amount of DOX released from FeHA in the absence of PEMF (about 3 wt% of the initial DOX loaded) was achieved after 2 days since no significant difference was found with the drug released after 3 and 6 days. The lower amount of drug released from FeHA with respect to HA is in good agreement with the higher affinity of DOX for FeHA, as already mentioned in the discussion on the adsorption isotherms.

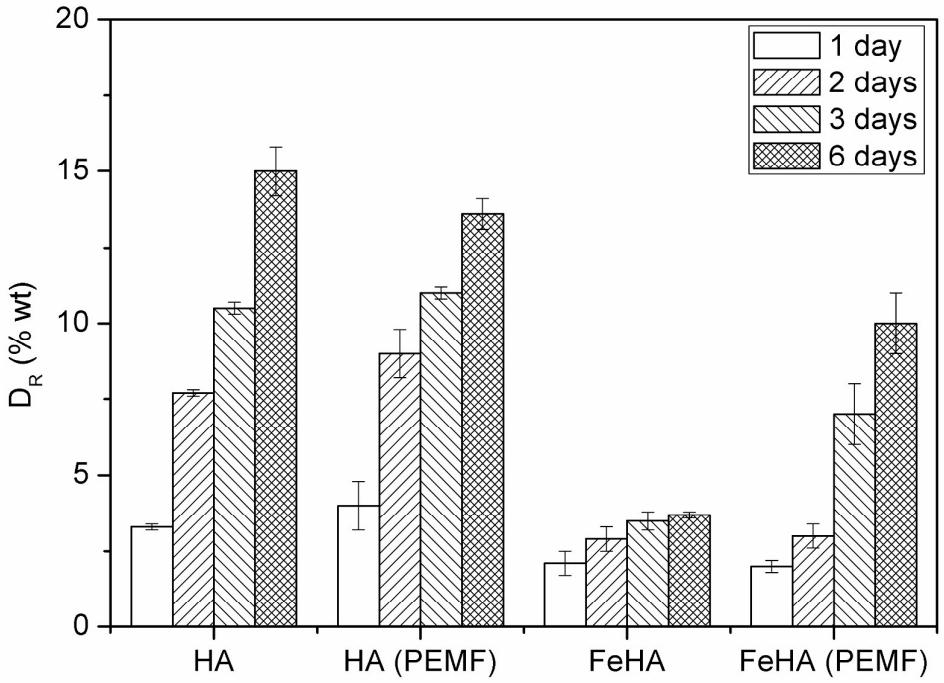

Figure 4. Kinetics of DOX release from HA and FeHA without and in the presence of pulsed electromagnetic field (PEMF).

Generally speaking, the relatively low amounts of DOX released from HA and FeHA at pH 7.4 are in agreement with the data previously reported in other works[58, 67] and confirms the strength of the binding between the apatite substrate and the drug molecules. The possibility to move FeHA NPs (and even entire cells after their internalization) under the application of a static magnetic field of 320 mT (Figure S8, ESI) has been recently reported,[68] corroborating their potential ability to be targeted in specific body systems by magnetic field. The high affinity of FeHA towards DOX and the low amount of the drug released at pH 7.4 points out that even FeHA-DOX could be guided without any concomitant loss of the therapeutic agent.

Magnetic NPs can be directed by static magnetic fields, but also provide remote controlled release of drugs or biomolecules, i.e. in scaffolds formulation by magnetic stimulation. Therefore the release of DOX from FeHA, in comparison with that from HA, has been evaluated applying a low frequency PEMF. Interestingly, in the presence of PEMF, the extent of DOX released from FeHA after 3 and 6 days increased significantly (3.5±0.3 vs 7.0±1.0 %wt after 3 days and 3.7±0.1 vs 10.0±1.0 %wt after 6 days, in absence and in presence of PEMF, respectively). This increase was directly related to the superparamagnetic feature of FeHA, since no statistical difference between DOX released from HA in presence and in absence of PEMF was observed.

It was well demonstrated in the last years that upon application of an alternating electromagnetic field, superparamagnetic NPs could generate local internal heating, causing structure disassembling and allowing the cargo (drug) to be released.[69, 70] In order to assess if a similar effect has occurred in this work, dissolution of FeHA in the presence or absence of PEMF was monitored. The extent of released Ca^{2+}, which can be considered as an index of the FeHA dissolution, was quantified after 3 and 6 days (Figure S9, ESI). No significant differences were observed between the amount of Ca^{2+} released in the presence or absence of PEMF, indicating that the increase of DOX released was not triggered by a more rapid degradation of the carriers. Moreover, during the PEMF exposure, FeHA suspension did not show any significant increase in temperature in the bulk solution. The PEMF used in this work was of low frequency comparable to that commercially used to stimulate and activate bone healing[71] and according to previous magnetic characterizations,[29] it was too weak to induce hyperthermia effect on FeHA. Therefore, the higher release of DOX from FeHA in the presence of PEMF can presumably be explained by the mechanical movement (i.e. shaking and flipping) of superparamagnetic NPs breaking the binding with the drug or allowing detachment of multi-molecular DOX assemblies from the NPs surface, rather than the destabilization of the crystal structure or the increase of temperature. This hypothesis is coherent with the fact that the appreciable differences of drug release in comparison to the experiments carried out without PEMF were evident only at long time points (i.e. 3 and 6 days) when the strong binding between drug and NPs was weakened by the continuous pulsed stimulation.

The DOX release kinetics data obtained for both HA and FeHA (whether in the absence or presence of PEMF) were analyzed from a mathematical viewpoint by fitting with several release models (zero order, first order, gas-like desorption, Higuchi, Korsmeyer-Peppas (KP) and Hixson-Crowell (HC) models), described in the literature.[72-74] A screening of these models was done using their linearized forms and considering the same number of data points to get

comparable R^2 correlation coefficients based on the same number of degrees of freedom (the origin (0;0) was omitted here due to logarithmic calculations tending to infinity in some of the models). The obtained correlation coefficients are listed in the Table S2, ESI. The results systematically indicate that the diffusion-based models, i.e. Higuchi and KP, were the most appropriate to fit the experimental release data, within the models tested. In contrast, only a poor correlation was found for gas-like desorption (model supposing a low adsorbent-adsorbate affinity) or matrix-dissolution model like HC. These results suggest that the release kinetics of DOX from HA or FeHA are mainly controlled by DOX diffusion from the substrate (inter)granular surfaces/spaces up to the solution rather than by the progressive dissolution of the substrates (which is indeed expected to be limited at physiological pH). The KP model is described by a power law of the form $D_R = k \cdot t^n$ where D_R is the cumulative release described above, "t" is the time, and "k" and "n" are constants (Higuchi model being a special case of KP with n = 0.5). The exponential factor "n" was found to vary in the range 0.29-0.86 (Table 2, ESI). Except for the unusually low value of 0.29 (lower than 0.5 and thus probably not representative), all other cases fall in the $0.5 \leq n \leq 1.0$ domain often considered as "anomalous transport", corresponding to complex release mechanisms with non-Fickian diffusivity. A similar situation was for example found in the case of vancomycin release from brushite.[75] It may be noted that no clear trend allows here distinguishing the release mechanisms of the different conditions studied (HA or FeHA; with or without PEMF application); only the amount of DOX released seems to be affected.

3.5 In vitro cell culture

Assessment of SAOS-2 cells viability grown in contact with 10 and 100 μM of DOX, either free or loaded onto HA and FeHA NPs, as well as with equivalent amounts of un-functionalized NPs, was carried out by quantification of metabolically active cells by the use of the MTT assay.[76] Results indicated that the DOX, loaded on HA and FeHA, was able to exert its cytotoxic activity on SAOS-2 cells. In fact, HA-DOX and FeHA-DOX, at all the concentrations tested (Table S1, ESI), showed reduced cell viability compared to the cells only sample, with statistic differences after 48 and 72 hours of culture (Figure 5). Moreover, no significant difference existed between the cytotoxic effect exerted by DOX free or loaded on HA and FeHA NPs at all the concentrations and each time points tested (Figure 5) indicating that the binding with the NPs did not affect the DOX antitumor activity.

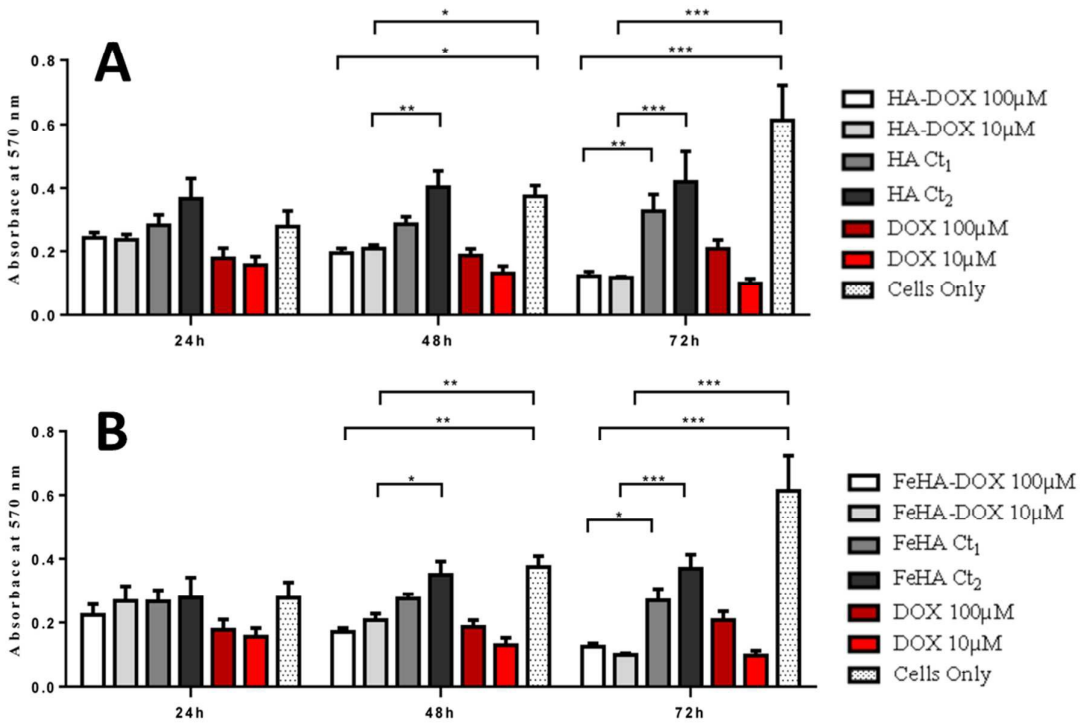

Figure 5. Analysis of SAOS-2 cell line viability by the MTT assay, after 24, 48 and 72 h of culture with 10 and 100 µM of DOX either free or loaded on (A) HA and (B) FeHA NPs, as well as with equivalent amounts of un-functionalized (A) HA and (B) FeHA. Cells-only were used as control. The graph shows the average and standard deviation of 6 replicates; statistical significant differences among the samples are indicated in the graphs: *p≤0.05, ** p≤0.01 and ***p≤0.001.

It is well reported that the calcium phosphate NPs can be internalized inside cells via clathrin- and caveolae-dependent endocytosis,[77] while free DOX can diffuse through the plasma membrane due its lipophilic properties.[78] Here, the nuclear localization of the different DOX-loaded HA and FeHA was evaluated by fluorescent microscopy. Figures 6 and 7 show DOX internalized without any difference among the groups. It was also possible to observe a higher intensity of florescence in both HA-DOX and FeHA-DOX 100 µM groups (Figure 6 and 7 A, B and C) compared to 10 µM groups (Figure 6 and 7 D, E and F), indicating a dose-dependent drug internalization. Moreover, in agreement with the data previously reported,[58, 67] in all the tested conditions, after 24 hours DOX was mainly detected within the nucleus.

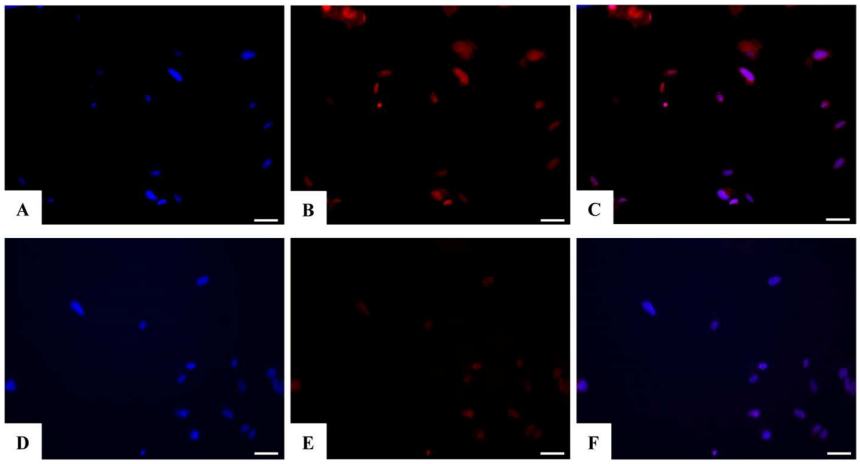

Figure 6. Analysis of the internalization of HA-DOX NPs in SAOS-2 cell line after 24 h of culture by fluorescence microscope. Images A, B and C show the sample HA-DOX 100 μM, respectively DAPI nuclear staining (blue), nuclear localization of DOX (red) and merge of the co-localization of DAPI and DOX. Images D, E and F show the sample HA-DOX 10 μM, respectively DAPI nuclear staining (blue), nuclear localization of DOX (red) and merge of the co-localization of DAPI and DOX. Scale bars 100 μm.

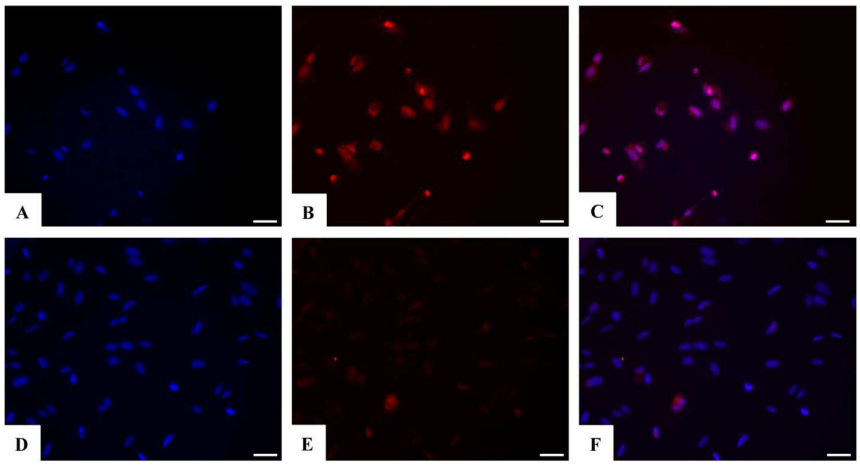

Figure 7. Analysis of the internalization of FeHA-DOX NPs in SAOS-2 cell line after 24 h of culture by fluorescence microscope. Images A, B and C show the sample FeHA-DOX 100 μM, respectively DAPI nuclear staining (blue), nuclear localization of DOX (red) and merge of the co-localization of DAPI and DOX. Images D, E and F show the sample FeHA-DOX 10 μM, respectively DAPI nuclear staining (blue), nuclear localization of DOX (red) and merge of the co-localization of DAPI and DOX. Scale bars 100μm.

On the basis of our previous data and those described in others works about the internalization of calcium phosphate NPs inside cells,[58, 67, 79, 80] and taking into account that the bind between DOX and HA/FeHA NPs was stable in physiological conditions, it is realistic to assume that DOX-loaded NPs were easily and rapidly internalized by cells and they were able to carry inside their bound DOX. Once inside the cells, DOX can be released from the NPs where the slightly acidic condition of lysosomes allowed a faster degradation of FeHA and HA NPs.[58, 67, 68] After that, DOX diffused into cell nucleus and induced DNA damage exerting its cell apoptosis effect. Several works reported that at initial stages free DOX is more effective than that attached to the iron oxide NPs due to the different mechanism of cellular uptake.[81, 82] Free DOX passes from the extracellular to the intracellular matrix by simple passive diffusion and reaches the nucleus easily, while in the case of iron oxide NPs-bound DOX, the drug is released from the NPs surface in lysosomes due to the acidic pH environment and hence DOX can reach the nucleus and intercalate DNA. The fact that in our case DOX coupled to apatitic NPs displayed comparable cytotoxicity of free DOX at all the time points was correlated with the fast internalization process and the rapid degradation of FeHA and HA in the lysosomal compartments respect to iron oxide NPs.

In vitro cells tests in presence of PEMF were not carried out because the time of magnetic field to trigger an higher drug release from FeHA (3 days) was not comparable to that of cell internalization (few hours), therefore any effect would be further appreciated.

4. Conclusions

In this work, the effective ability of previously synthesized superparamagnetic FeHA[29] to load DOX was demonstrated. FeHA displayed higher affinity for DOX in comparison to iron-free biomimetic HA NPs due to good affinity of the drug for the iron cations of FeHA surface. The stability of the binding between DOX and FeHA was stronger compared to HA; in fact, the quantity of DOX released at pH 7.4 from FeHA was lower than the drug released from HA. The release of DOX from FeHA was also assessed in the presence of PEMF, and fascinatingly the extent of DOX released after 3 and 6 days in these conditions increased significantly in comparison to the drug release without PEMF. This finding was explained by the mechanical shacking of superparamagnetic NPs breaking the binding with DOX or allowing detachment of drug assemblies from the NPs surface, rather than by some higher degradation of NPs or a temperature increase. Finally, *in vitro* assays demonstrated that DOX loaded on HA and FeHA was able to exert its cytotoxic activity on SAOS-2 cells at the same level as free DOX, for all the

concentrations and time points tested, because the functionalized NPs can be rapidly internalized within cells and release DOX, which accumulated in the nucleus and exerted cytotoxic activity.

In light of our results and taking into account that the biocompatibility of FeHA particles, their pH-dependent biodegradability, and their ability to be moved by an external magnetic field was already demonstrated,[29, 30, 68] and although further *in vitro* and *in vivo* studies are necessary, we can conclude that this new superparamagnetic nanosystem can represent a novel alternative to SPION to set up magnetic devices for stimulating personalized nanomedical applications such as targeted drug nano-carriers and scaffolds for bone tissue engineering with remotely controlled multi-functionalities.

Acknowledgments

We acknowledge support from the Italian Ministry for Education, University and Research (MIUR) in the framework of the Flagship Project NanoMax (PNR 201-2013), from the French Egide association (Hubert-Curien "Galilée" program, project #28285UB), and from the Università Italo-Francese (Programma Galileo 2012/2013). The authors also thank O. Marsan (CIRIMAT-Toulouse) and Yannick Coppel (LCC-Toulouse) for Raman and NMR technical support, respectively. The Biostim SPT pulse generator was kindly provided by IGEA (Carpi, Italy).

References

1. K. Fuhrmann, M. A. Gauthier and J.-C. Leroux, *Mol. Pharmaceut.*, 2014, **11**, 1762-1771.
2. J. M. Coburn and D. L. Kaplan, *Bioconjugate Chem.*, 2015, **26**, 1212–1223.
3. S. Pietronave, M. Iafisco, D. Locarno, L. Rimondini and M. Prat, *J. Appl. Biomater. Biomech.*, 2009, **7**, 77-89.
4. T. Sun, Y. S. Zhang, B. Pang, D. C. Hyun, M. Yang and Y. Xia, *Angew. Chem., Int. Ed.*, 2014, **53**, 12320-12364.
5. K. Yan, P. Li, H. Zhu, Y. Zhou, J. Ding, J. Shen, Z. Li, Z. Xu and P. K. Chu, *RSC Advances*, 2013, **3**, 10598-10618.
6. L. H. Reddy, J. L. Arias, J. Nicolas and P. Couvreur, *Chem. Rev.*, 2012, **112**, 5818-5878.
7. M. Arruebo, R. Fernández-Pacheco, M. R. Ibarra and J. Santamaría, *Nano Today*, 2007, **2**, 22-32.
8. J. Kolosnjaj-Tabi, C. Wilhelm, O. Clement and F. Gazeau, *J. Nanobiotechnol.*, 2013, **11**, S7.

9. A. Ranzoni, G. Sabatte, L. J. van Ijzendoorn and M. W. J. Prins, *ACS Nano*, 2012, **6**, 3134-3141.

10. S. H. Lee, B. H. Kim, H. B. Na and T. Hyeon, *Wiley Interdiscip. Rev.: Nanomed. Nanobiotechnol.*, 2014, **6**, 196-209.

11. T. Kobayashi, *Biotechnol. J.*, 2011, **6**, 1342-1347.

12. J. Meng, B. Xiao, Y. Zhang, J. Liu, H. Xue, J. Lei, H. Kong, Y. Huang, Z. Jin, N. Gu and H. Xu, *Sci. Rep.*, 2013, **3**.

13. J.-J. Kim, R. K. Singh, S.-J. Seo, T.-H. Kim, J.-H. Kim, E.-J. Lee and H.-W. Kim, *RSC Advances*, 2014, **4**, 17325-17336.

14. H.-Y. Xu and N. Gu, *Front. Mater. Sci.*, 2014, **8**, 20-31.

15. R. Sensenig, Y. Sapir, C. MacDonald, S. Cohen and B. Polyak, *Nanomedicine*, 2012, **7**, 1425-1442.

16. T. Neuberger, B. Schöpf, H. Hofmann, M. Hofmann and B. von Rechenberg, *J. Magn. Magn. Mater.*, 2005, **293**, 483-496.

17. A. Singh and S. K. Sahoo, *Drug Discovery Today*, 2014, **19**, 474-481.

18. C. Xu and S. Sun, *Adv. Drug. Deliver. Rev.*, 2013, **65**, 732-743.

19. F. M. Kievit and M. Zhang, *Acc. Chem. Res.*, 2011, **44**, 853-862.

20. M. Mahmoudi, S. Sant, B. Wang, S. Laurent and T. Sen, *Adv. Drug. Deliver. Rev.*, 2011, **63**, 24-46.

21. N. Singh, G. J. S. Jenkins, R. Asadi and S. H. Doak, *Nano Rev.*, 2010, **1**, 5358.

22. J.-E. Kim, J.-Y. Shin and M.-H. Cho, *Arch. Toxicol.*, 2012, **86**, 685-700.

23. T. K. Jain, M. K. Reddy, M. A. Morales, D. L. Leslie-Pelecky and V. Labhasetwar, *Mol. Pharmaceut.*, 2008, **5**, 316-327.

24. J. Huang, L. Bu, J. Xie, K. Chen, Z. Cheng, X. Li and X. Chen, *ACS Nano*, 2010, **4**, 7151-7160.

25. M.-T. Zhu, W.-Y. Feng, Y. Wang, B. Wang, M. Wang, H. Ouyang, Y.-L. Zhao and Z.-F. Chai, Toxicol. Sci., 2009, **107**, 342-351.

26. J. Gómez-Morales, M. Iafisco, J. M. Delgado-López, S. Sarda and C. Drouet, *Prog. Cryst. Growth Charact. Mater.*, 2013, **59**, 1-46.

27. E. Boanini, M. Gazzano and A. Bigi, *Acta Biomater.*, 2010, **6**, 1882-1894.

28. M. Šupová, *Ceram. Int.*, 2015, **41**, 9203-9231

29. A. Tampieri, T. D'Alessandro, M. Sandri, S. Sprio, E. Landi, L. Bertinetti, S. Panseri, G. Pepponi, J. Goettlicher, M. Bañobre-López and J. Rivas, *Acta Biomater.*, 2012, **8**, 843-851.

30. S. Panseri, C. Cunha, T. D'Alessandro, M. Sandri, G. Giavaresi, M. Marcacci, C. T. Hung and A. Tampieri, *J. Nanobiotechnol.*, 2012, **10**, 32

31. M. Iafisco, M. Sandri, S. Panseri, J. M. Delgado-López, J. Gómez-Morales and A. Tampieri, *Chem. Mater.*, 2013, **25**, 2610-2617.

32. A. Gloria, T. Russo, U. D'Amora, S. Zeppetelli, T. D'Alessandro, M. Sandri, M. Bañobre-López, Y. Piñeiro-Redondo, M. Uhlarz, A. Tampieri, J. Rivas, T. Herrmannsdörfer, V. A. Dediu, L. Ambrosio and R. De Santis, *J. R. Soc., Interface*, 2013, **10**.

33. O. Tacar, P. Sriamornsak and C. R. Dass, *J. Pharm. Pharmacol.*, 2013, **65**, 157-170.

34. Y. Octavia, C. G. Tocchetti, K. L. Gabrielson, S. Janssens, H. J. Crijns and A. L. Moens, *J. Mol. Cell Cardiol*, 2012, **52**, 1213-1225.

35. G. Aubel-Sadron and D. Londos-Gagliardi, *Biochimie*, 1984, **66**, 333-352.

36. S. Cazalbou, G. Bertrand and C. Drouet, *J. Phys. Chem. B*, 2015, **119**, 3014-3024.

37. P. Pascaud, P. Gras, Y. Coppel, C. Rey and S. Sarda, *Langmuir*, 2013, **29**, 2224-2232.

38. H. Autefage, F. Briand-Mesange, S. Cazalbou, C. Drouet, D. Fourmy, S. Goncalves, J. P. Salles, C. Combes, P. Swider and C. Rey, *J. Biomed. Mater. Res. B,* 2009, **91B**, 706-715.

39. A. L. Patterson, *Phys. Rev.*, 1939, **56**, 978-982.

40. L. Fassina, L. Visai, F. Benazzo, L. Benedetti, A. Calligaro, M. G. Cusella De Angelis, A. Farina, V. Maliardi and G. Magenes, *Tissue Eng.*, 2006, **12**, 1985-1999.

41. C. Rey, C. Combes, C. Drouet, H. Sfihi and A. Barroug, *Mater. Sci. Eng., C*, 2007, **27**, 198-205.

42. R. Z. LeGeros, R. Kijkowska, C. Bautista and J. P. Legeros, *Connect. Tissue Res.*, 1995, **33**, 203-209.

43. M. Iafisco, M. Marchetti, J. Gómez Morales, M. a. A. Hernández-Hernández, J. M. García Ruiz and N. Roveri, *Cryst. Growth Des.*, 2009, **9**, 4912-4921.

44. J. M. Delgado-López, M. Iafisco, I. Rodríguez, A. Tampieri, M. Prat and J. Gómez-Morales, *Acta Biomater.*, 2012, **8**, 3491-3499.

45. S. Koutsopoulos, *J. Biomed. Mater. Res.*, 2002, **62**, 600-612.

46. X. Ma and D. E. Ellis, *Biomaterials*, 2008, **29**, 257-265.

47. C. Rey, C. Combes, C. Drouet, S. Cazalbou, D. Grossin, F. Brouillet and S. Sarda, *Prog. Cryst. Growth Charact. Mater.,* 2014, **60**, 63-73.

48. T. Ito, L. Sun, M. A. Bevan and R. M. Crooks, *Langmuir*, 2004, **20**, 6940-6945.

49. F.-C. Wu, R.-L. Tseng and R.-S. Juang, *Chem. Eng. J.*, 2009, **150**, 366-373.

50. C. Aharoni and F. C. Tompkins in *Advances in Catalysis and Related Subjects*, ed. D. D. Eley, H. Pines and P. B. Weisz, Academic Press, New York, 1970, **21**, 1–49.

51. L. E. Gerweck, S. V. Kozin and S. J. Stocks, *Br. J. Cancer*, 1999, **79**, 838-842.

52. Z. Fülöp, R. Gref and T. Loftsson, *Int. J. Pharm.*, 2013, **454**, 559-561.

53. L. Benaziz, A. Barroug, A. Legrouri, C. Rey and A. Lebugle, *J. Colloid Interface Sci.*, 2001, **238**, 48-53.

54. K. Achelhi, S. Masse, G. Laurent, A. Saoiabi, A. Laghzizil and T. Coradin, *Dalton Trans.*, 2010, **39**, 10644-10651.

55. L. K. Koopal, W. H. van Riemsdijk, J. C. M. de Wit and M. F. Benedetti, *J. Colloid Interface Sci.*, 1994, **166**, 51-60.

56. Q. Luo and J. D. Andrade, *J. Colloid Interface Sci.*, 1998, **200**, 104-113.

57. M. Choimet, A. Tourrette and C. Drouet, *J. Colloid Interface Sci.*, 2015, **456**, 132-137.

58. I. Rodríguez-Ruiz, J. M. Delgado-López, M. A. Durán-Olivencia, M. Iafisco, A. Tampieri, D. Colangelo, M. Prat and J. Gómez-Morales, *Langmuir*, 2013, **29**, 8213-8221.

59. A. Al-Kattan, F. Errassifi, A. M. Sautereau, S. Sarda, P. Dufour, A. Barroug, I. D. Santos, C. Combes, D. Grossin, C. Rey and C. Drouet, *Adv. Eng. Mater.*, 2010, **12**, B224-B233.

60. M. Iafisco, B. Palazzo, G. Martra, N. Margiotta, S. Piccinonna, G. Natile, V. Gandin, C. Marzano and N. Roveri, *Nanoscale*, 2012, **4**, 206-217.

61. E. Hayakawa, K. Furuya, T. Kuroda, M. Moriyama and A. Kondo, *Chem. Pharm. Bull.*, 1991, **39**, 1282-1286.

62. R. Anand, S. Ottani, F. Manoli, I. Manet and S. Monti, *RSC Advances*, 2012, **2**, 2346-2357.

63. H. Cortes-Funes, M. Gosalvez, A. Moyano, A. Mañas and C. Mendiola, *Cancer Treat. Rep.*, 1979, **63**, 903-908.

64. M. Gosálvez, M. F. Blanco, C. Vivero and F. Vallés, *Eur. J. Cancer*, 1978, **14**, 1185-1190.

65. P. M. May, G. K. Williams and D. R. Williams, *Inorg. Chim. Acta*, 1980, **46**, 221-228.

66. S. Kayal and R. V. Ramanujan, *Mater. Sci. Eng., C,* 2010, **30**, 484-490.

67. M. Iafisco, J. M. Delgado-Lopez, E. M. Varoni, A. Tampieri, L. Rimondini, J. Gomez-Morales and M. Prat, *Small*, 2013, **9**, 3834-3844.

68. S. Panseri, M. Montesi, M. Sandri, M. Iafisco, A. Adamiano, M. Ghetti, G. Cenacchi and A. Tampieri, *J. Biomed. Nanotech.*, accepted.

69. C. R. Thomas, D. P. Ferris, J.-H. Lee, E. Choi, M. H. Cho, E. S. Kim, J. F. Stoddart, J.-S. Shin, J. Cheon and J. I. Zink, *J. Am. Chem. Soc.*, 2010, **132**, 10623-10625.

70. S. Brulé, M. Levy, C. Wilhelm, D. Letourneur, F. Gazeau, C. Ménager and C. Le Visage, *Adv. Mat.*, 2011, **23**, 787-790.

71. L. Massari, G. Caruso, V. Sollazzo and S. Setti, *Clin. Cases Miner. Bone Metab.*, 2009, **6**, 149-154.

72 M. Barzegar-Jalali, K. Adibkia, H. Valizadeh, M.R.S. Shadbad, A. Nokhodchi, Y. Omidi, G. Mohammadi, S.H. Nezhadi and M. Hasan, *J. Pharm. Pharm. Sci.*, 2008, **11**, 167-177.

73 C.G. Weber, M. Mueller, N. Vandecandelaere, I. Trick, A. Burger-Kentischer, T. Maucher and C. Drouet, *J. Mater. Sci. Mater. Med.*, 2014, **25**, 595-606.

74 N.L. Ignjatovic, P. Ninkov, R. Sabetrasekh and D.P. Uskokovic, *J. Mater. Sci. Mater. Med.*, 2010, **21**, 231-239

75 U. Gbureck, E. Vorndran and J.E. Barralet, *Acta Biomater.*, 2008, **4**, 1480-1486.

76. Y. Liu, D. A. Peterson, H. Kimura and D. Schubert, *J. Neurochem.*, 1997, **69**, 581-593.

77. D. Y. E. Olton, J. M. Close, C. S. Sfeir and P. N. Kumta, *Biomaterials*, 2011, **32**, 7662-7670.

78. A. Beljebbar, G. D. Sockalingum, J. F. Angiboust and M. Manfait, *Spectrochim. Acta, Part A*, 1995, **51**, 2083-2090.

79. S. P. Victor, W. Paul, M. Jayabalan and C. P. Sharma, *CrystEngComm*, 2014, **16**, 9033-9042.

80. Y.-H. Yang, C.-H. Liu, Y.-H. Liang, F.-H. Lin and K. C. W. Wu, *J. Mater. Chem. B*, 2013, **1**, 2447-2450.

81. K. Tomankova, K. Polakova, K. Pizova, S. Binder, M. Havrdova, M. Kolarova, E. Kriegova, J. Zapletalova, L. Malina, J. Horakova, J. Malohlava, A. Kolokithas-Ntoukas, A. Bakandritsos, H. Kolarova and R. Zboril, *Int. J. Nanomedicine*, 2015, **10**, 949-961.

82. M. I. Majeed, Q. Lu, W. Yan, Z. Li, I. Hussain, M. N. Tahir, W. Tremel and B. Tan, *J. Mater. Chem. B*, 2013, **1**, 2874-2884.

Graphical Abstract

Iron-doped superparamagnetic apatite nanoparticles are promising materials for magnetic drug delivery systems due to their ability to strongly bind the anticancer doxorubicin, and to provide an active control over the drug release by using a low-frequency pulsed electromagnetic field.

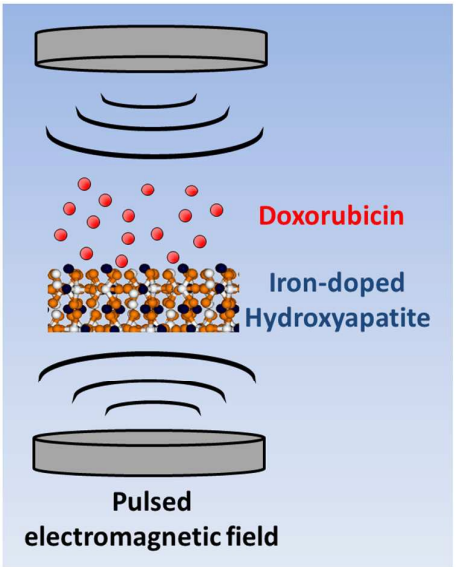

Iron-doped superparamagnetic apatite nanoparticles are promising materials for magnetic drug delivery systems due to their ability to strongly bind the anticancer doxorubicin, and to provide an active control over the drug release by using a low-frequency pulsed electromagnetic field

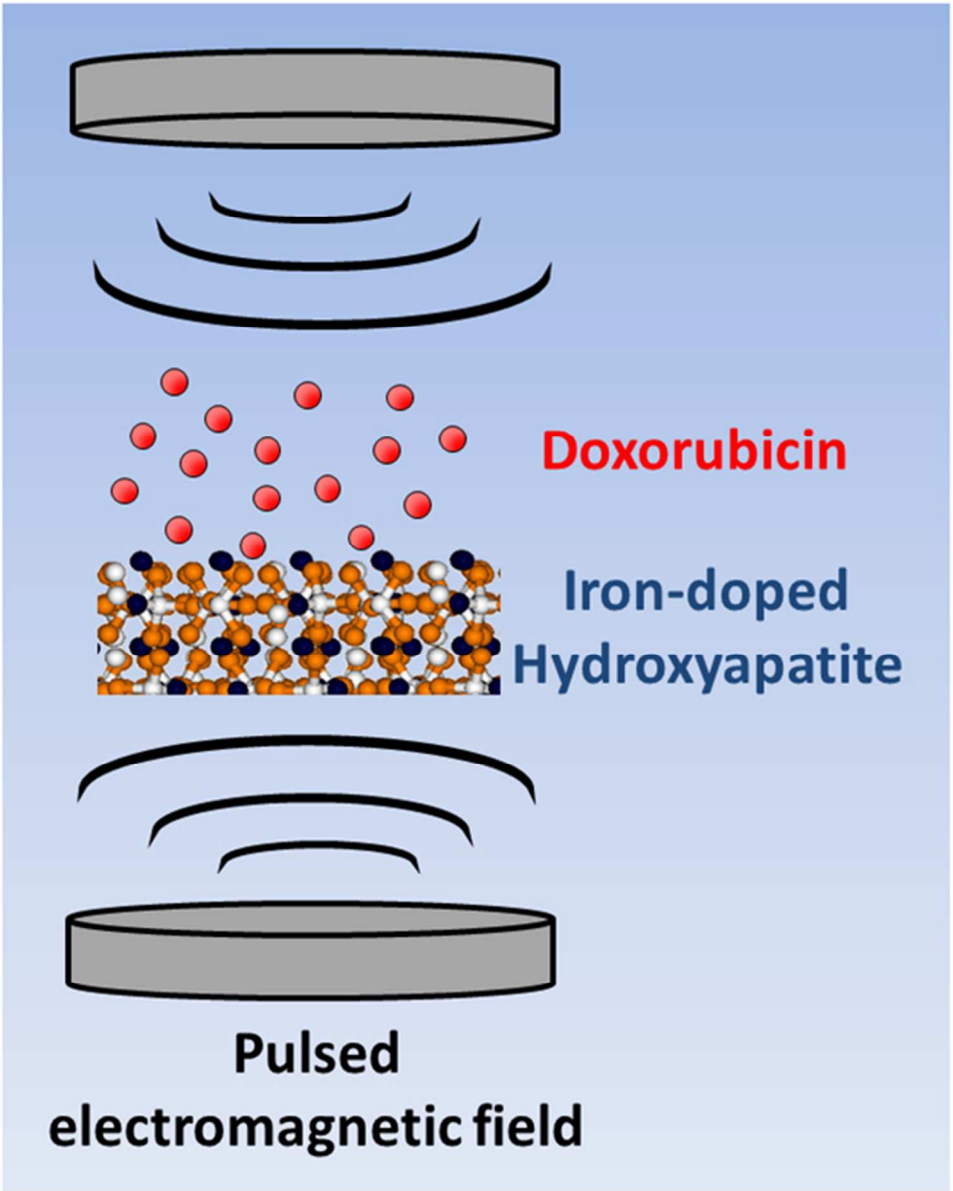

106x133mm (150 x 150 DPI)